



School of Mechanical and Manufacturing Engineering

Faculty of Engineering

UNSW Sydney

BY

Pierce Boughton

**Attitude Control of Solar Sail with Reflectivity Control
Devices**

Submitted: 26/04/2025	Student zID: z5308771
Supervisor: Yang Yang	

ORIGINALITY STATEMENT

"I hereby declare that this submission is my own work and to the best of my knowledge it contains no materials previously published or written by another person, or substantial proportions of material which have been accepted for the award of any other degree or diploma at UNSW or any other educational institution, except where due acknowledgement is made in the thesis. Any contribution made to the research by others, with whom I have worked at UNSW or elsewhere, is explicitly acknowledged in the thesis. I also declare that the intellectual content of this thesis is the product of my own work, except to the extent that assistance from others in the project's design and conception or in style, presentation and linguistic expression is acknowledged."

Signed: P. B. A.

Date: 25/04/25

Abstract

Solar sails offer a promising solution for fuel-free propulsion, enabling novel mission profiles and deeper space exploration. As spacecraft become lighter, the advantages of solar sailing grow. While reaction wheels are standard for satellite attitude control, the high moment of inertia of solar sails often lead to frequent reaction wheel saturation, necessitating momentum offloading via magnetorquers and disruptive tumbling manoeuvres. This study investigates Reflectivity Control Devices (RCDs) as an alternative method for momentum management, aiming to eliminate the need for tumbling. A dynamic model of a solar sail in sun-synchronous orbit is developed, incorporating disturbance torques to assess control effectiveness. Numerical simulations evaluate the effectiveness of RCDs in offloading reaction wheel momentum and preventing saturation.

1 Introduction

Solar Radiation Pressure (SRP) is known as one of the most significant environmental disturbances in space and must be considered in mission design [1]. Since photons are known to have momentum, a pressure is exerted upon objects in sunlight. If the photon is absorbed, the momentum from the photon is also absorbed. Sunlight may also be reflected, which doubles the pressure force experienced as shown in Fig. 1 below. The concept of solar sailing is to utilise the SRP as a source of propulsion for orbital manoeuvres and attitude adjustment in place of or alongside typical propulsion systems typically used by spacecraft like thrusters.

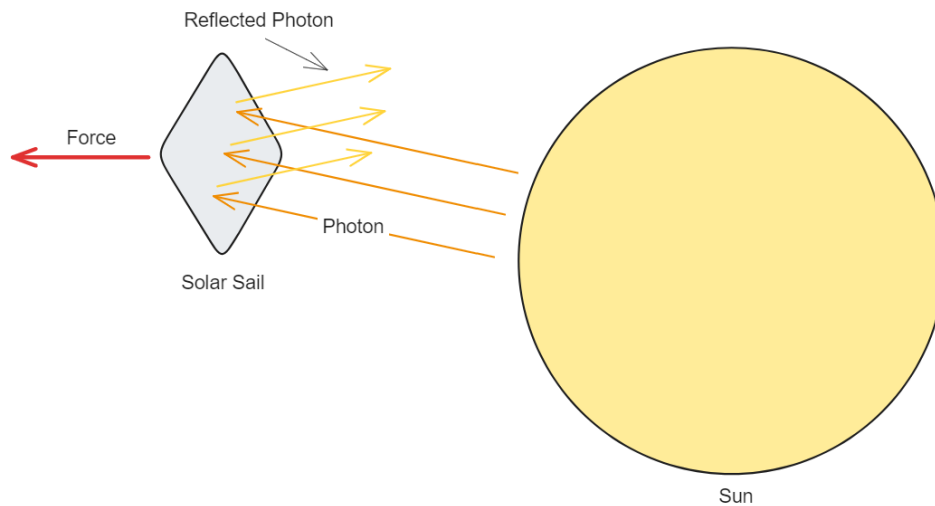


Figure 1. Solar sailing concept utilising solar radiation pressure for propulsion

To maximise the resulting force, surface area needs to be maximised while mass is minimised. The sail is initially stowed to reduce the spacecraft size during launch. Once in space, a solar sail consisting of a thin, reflective sheet is deployed, increasing the surface area of the spacecraft and maximising SRP.

This paper highlights some key solar sail missions (section 1.1) and methods of solar sail attitude control (section 1.2-1.3). The development of the solar sail model is included in section 2 and the results are presented and discussed in section 3.

1.1 History

The term solar sailing was coined by Richard L. Garwin in 1958 [2] following previous concepts dating back to the 17th century. Early designs envisioned massive sails to propel heavy spacecraft. Over time, however, the emphasis shifted toward smaller, more efficient missions that could demonstrate the technology with manageable risk.

IKAROS

JAXA's IKAROS mission [3], [4] used a 200 m² sail attached to a 307 kg spacecraft. Instead of large, rigid booms, the mission employed a spinning sail to increase the area-to-mass ratio. Crucially, IKAROS featured Reflectivity Control Devices (RCDs), activated in a timed manner during the spin to create an imbalance in SRP, generating the required torques to adjust attitude. Many missions since IKAROS have not considered the use of RCD technology for attitude control, even with its simplicity and little mass addition.

LightSail 2

The LightSail 2 mission [5], [6] employed a single-axis reaction wheel along with magnetorquers to perform rapid slews, alternating between “thrust-on” (sail normal parallel to

the sun-vector) and “thrust-off” (sail normal perpendicular to the sun-vector) configurations. This strategy maximized SRP at key orbital points. However, LightSail 2 encountered issues with reaction wheel saturation that necessitated frequent momentum dumping using magnetorquers. As a result, the solar sail’s altitude decayed, eventually leading to re-entry after about three years. Although effective in demonstrating controlled solar sailing, these challenges illustrate the limits of current attitude control systems for missions requiring precise pointing, such as Earth observation.

1.2 Solar Sail Attitude Control

Sunflower Mission

The Sunflower mission concept [7] proposed a pyramid-shaped solar sail designed to passively maintain a sun-pointing orientation using the angular dependence of SRP on diffusive surfaces. This approach eliminates the need for active control in two axes, reducing onboard power and actuator demands. However, the proposed mission requires large, rapid slews for orbit changes, which can lead to frequent reaction wheel saturation. Additionally, no complex-geometry solar sails have flight heritage, and the risks associated with their deployment and dynamic behaviour remain untested. As such, these configurations are considered high-risk compared to simpler, flat-rigid sail designs with demonstrated in-orbit performance.

CubeSail

The CubeSail mission [8] aimed to demonstrate 3-axis attitude control using a combination of magnetorquers and a two-dimensional translation unit that adjusted the centre of mass relative to the centre of pressure. While mass-efficient and mechanically simple, the mission suffered a critical communications failure before full validation. Simulations indicated limited pointing accuracy, with attitude errors exceeding five degrees during slews, which is insufficient for precision tasks such as Earth observation. Though conceptually promising, CubeSail highlights the challenges of non-traditional attitude control schemes and the need for additional actuators to meet stricter pointing requirements.

Control Vanes and Sliding Mass

Bo Fu’s state-of-the-art survey [9] states that conventional attitude control systems are insufficient for use with solar sails due to the increase in disturbance torques. Bo Fu highlights two mechanically driven approaches for solar sail attitude control: control vanes, which rotate small panels at the sail’s periphery to shift the SRP centre-of-pressure and generate torque, and sliding-mass systems, where weights (often the payload itself) translate along booms to alter the centre-of-mass position. While control vanes offer redundancy and fine attitude adjustment, they introduce deployment complexity, hinge mechanism mass, and additional points of failure. Sliding-mass actuators similarly demand precise motors and structural reinforcement, increasing system mass and risking oscillations during motion. Neither method has yet flown on a solar sail, and their unproven in-orbit reliability make them high-risk.

1.3 Reflectivity Control Devices

In previous solar sail missions, the large mass moment of inertia of the sail has provided some challenges with attitude control [6]. Reaction wheels suffer from saturation due to the increase in disturbance torques and additional control requirements [9]. Offloading of the reaction wheel momentum can be achieved through momentum dumping, requiring the spacecraft to undertake tumbling and then detumbling using magnetorquers. However, frequent momentum dumping in this manner can be detrimental to the mission as control during this time is limited. RCDs are explored as a solution to this.

RCDs are thin flexible membranes, placed on the surface of a solar sail to change the reflective properties of the sail with an applied voltage. RCDs contain liquid crystal, which allow the device to change between specular reflection and diffusive reflection [3]. Since the SRP force is dependent on the reflective properties, by changing the reflectivity state of different areas of the sail, a torque is created, allowing for attitude control of the spacecraft as shown in Fig. 2 below.

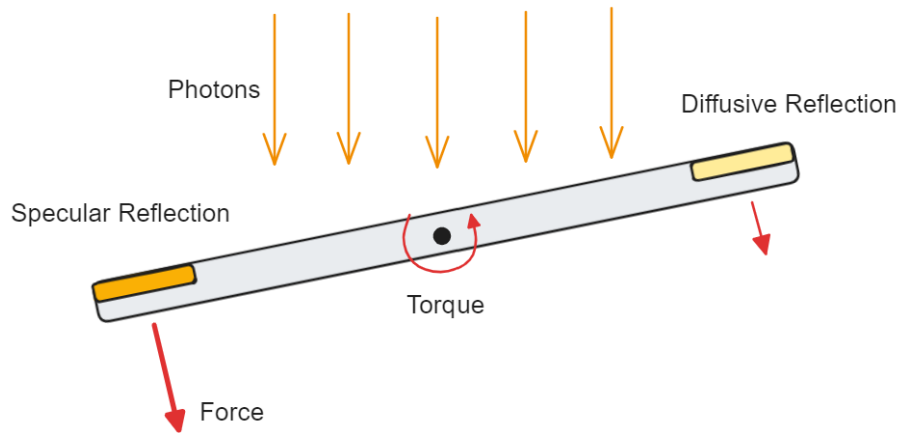


Figure 2. RCD solar sail torque for attitude control. Specular reflection produces more force than diffusive reflection resulting in a torque being produced.

RCDs offer a simple and lightweight approach to attitude control for solar sails. They are one of the few successfully demonstrated attitude control devices for solar sails but are yet to be demonstrated with a rigid, non-spinning solar sail in an Earth-orbit. With advancing structural boom technology [10], higher area-to-mass ratios are being achieved with rigid sails, leading to larger adoption of rigid sails over spinning sails. Although RCD technology is limited to 2-axis control, it is relatively simple to implement, with no additional mechanisms or mechanical design complexity, decreasing the risk of failure. Since Z-axis disturbance torques are typically the lowest [11], RCDs can be used in addition to three reaction wheels to offload momentum from the X-aligned and Y-aligned reaction wheels, preventing early saturation.

1.4 Reference Frames

The following are some commonly used reference frames that will be referred to throughout the remainder of the paper.

ICRF

The International Celestial Reference Frame (ICRF) is an inertial reference frame with its origin at the centre of the Earth. This frame is used for position and velocity throughout the models. It is treated as equal to the ECI coordinate system realised at J2000 [12].

LVLH

The Local Vertical, Local Horizontal frame is a rotating frame centred on the spacecraft, useful for describing the orientation of a spacecraft in orbit. Its x-axis is defined as the spacecraft position vector from the Earth. Its y-axis completes the right-hand coordinate system and points in the direction of the velocity vector for circular orbits. Its z-axis is defined as pointing normal to the orbital plane [12].

Body-Frame

The body coordinate frame is a non-inertial reference frame fixed to the body of the spacecraft. This is shown in Fig. 3 below.

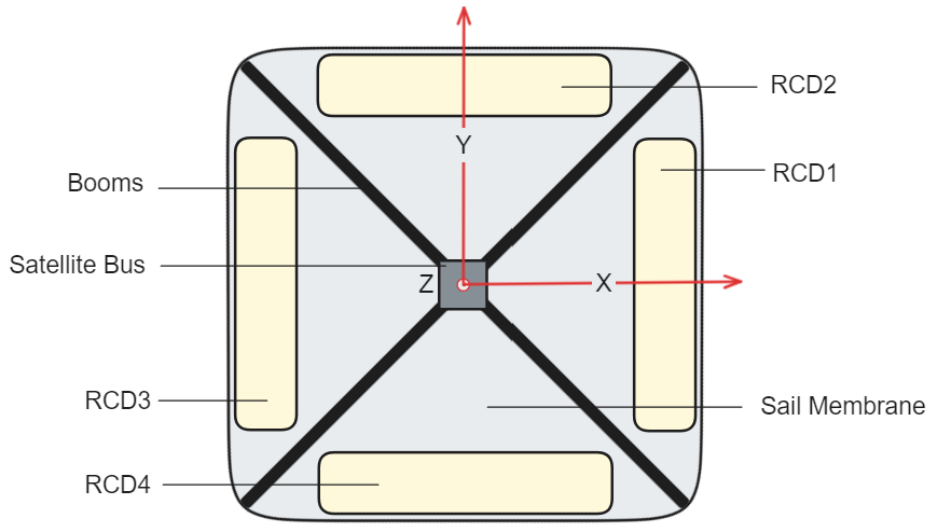


Figure 3. Solar sail RCD layout and body axes. Z-axis completes right-hand coordinate system (out of page). Not to scale.

1.5 Disturbance Torques

Only four disturbance torques are consequential for a typical Earth-orbiting spacecraft [1]: gravity gradient, magnetic field torques, SRP torque and atmospheric drag torque. SRP torque is the most significant for solar sail applications and is the result of an offset between the centre of pressure and the centre of mass. Inconsistent surface properties or multiple surfaces with different angles result in the centre of pressure changing and a torque being created. Atmospheric Drag torque works in a comparable manner to SRP torque. When the centre of atmospheric drag pressure (somewhere on the ram area) is not aligned with the centre of mass, a torque is created [1]. Gravity gradient torque is created when the centre of gravity is not aligned with the centre of mass of the spacecraft [1]. Since gravity is a function of the altitude of the spacecraft, the force of gravity is not consistently applied over the spacecraft, resulting in a centre of gravity that is offset from the centre of mass. A magnetic field torque is created when the residual magnetic moment of a spacecraft does not align with Earth's magnetic field. The magnetic torque will attempt to align the magnetic fields of the spacecraft and the Earth [1].

2 Solar Sail Model

2.1 Overview of System

Solar sail models have been developed to test the effectiveness of RCDs at offloading momentum from the reaction wheels and preventing saturation. The solar sails were modelled to be in a Sun-Synchronous orbit, typically used for Earth observation [13], ensuring consistent exposure to sunlight. Initial detumbling, and deployment of the solar sail are outside the scope of this paper and are not modelled.

Two models have been developed, henceforth referred to as model A and model B. Model A relies solely on the use of reaction wheels for attitude control, maintaining an Earth-pointing orientation. An overview of the control system for model A is shown in Fig. 4 below.

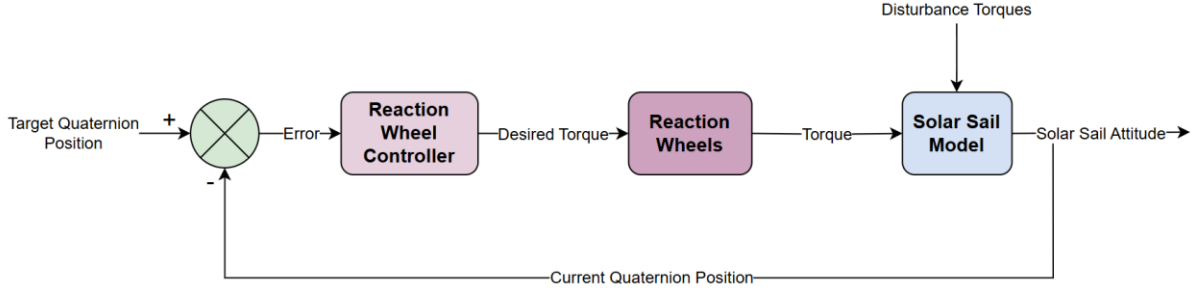


Figure 4. Model A attitude control system diagram

This is a typical feedback loop used for satellite attitude control. Note that the position and rotation of the solar sail are assumed to be known exactly, and no sensors or sensor inaccuracies have been modelled for simplicity. The error is calculated from the difference between the current orientation and the target orientation. This error is given to the reaction wheel controller, which calculates the desired torque signal for the reaction wheels. This desired torque is given to the reaction wheel actuators, which generate an actual torque that is dependent on the actuator limitations. This is then applied to the solar sail plant. Meanwhile, disturbance torques also act on the solar sail, which must be countered by the reaction wheels to maintain pointing.

Model B uses RCDs to offload momentum from the reaction wheels to prevent saturation from occurring. Two modes have been implemented in model B: Earth-pointing and Sun-Pointing. The nominal mode is Earth-pointing for completing mission objectives like observation, switching to Sun-pointing to maximise SRP and utilise the RCDs for momentum offloading. Once offloading is complete, the spacecraft will return to Earth-pointing. Note that the RCDs are only used in Sun-pointing mode. The control system for model B is shown in Fig. 5 below.

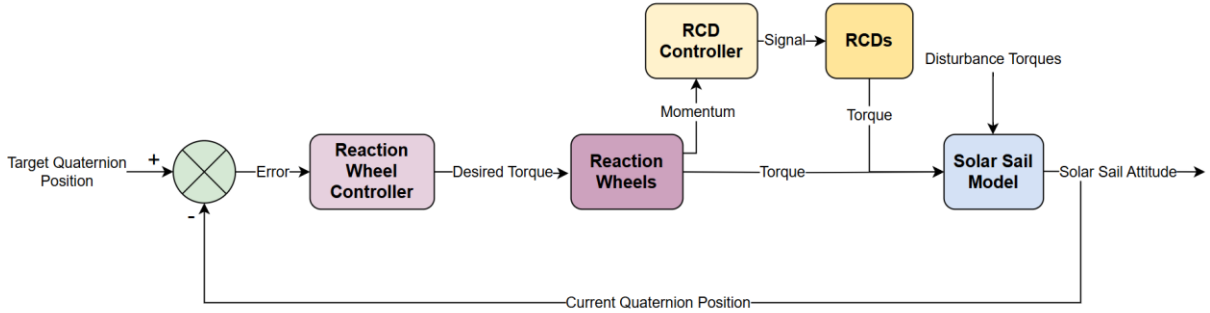


Figure 5. Model B attitude control system diagram

Fig. 5 additionally contains the ‘RCD Controller’ and the ‘RCDs’ blocks. The RCD controller commands each of the RCDs to be either ON or OFF to generate the required torque. The torque acts on the solar sail and is counteracted by the reaction wheels, reducing the wheel angular velocity and therefore momentum. The results from model B will be compared with those from model A to evaluate the effectiveness of model B.

2.2 Dynamics

Translational Dynamics

The spacecraft translational dynamics are governed by the following equation:

$$\mathbf{a} = \text{body2icrf} \left(\frac{\mathbf{F}_b}{m} \right) + \mathbf{a}_{\text{centralbody}} + \mathbf{a}_{\text{thirdbody}}, \quad (1)$$

where \mathbf{a} is the spacecraft acceleration, \mathbf{F}_b is the combined atmospheric drag and SRP force acting on the spacecraft body, m is the mass of the spacecraft, $\mathbf{a}_{centralbody}$ is the acceleration from Earth, and $\mathbf{a}_{thirdbody}$ is the acceleration from additional bodies.

\mathbf{F}_b is given by:

$$\mathbf{F}_b = \mathbf{F}_{drag} + \mathbf{F}_{SRP}, \quad (2)$$

where \mathbf{F}_{drag} is the atmospheric drag force in the body frame, and \mathbf{F}_{SRP} is the SRP force in the body frame. $\mathbf{a}_{centralbody}$ is determined using the EGM2008 Spherical harmonics gravitational potential model. $\mathbf{a}_{thirdbody}$ is determined using DE432t ephemeris data of the Sun and Moon, assuming point masses.

Rotational Dynamics

The spacecraft rotational dynamics are governed by the following equation [14]:

$$\boldsymbol{\alpha} = I^{-1}[\mathbf{M}_b + \boldsymbol{\tau}_b - \boldsymbol{\omega} \times (I\boldsymbol{\omega})], \quad (3)$$

where $\boldsymbol{\alpha}$ is the angular acceleration of the spacecraft in ICRF, \mathbf{M}_b is the torque from actuators (RCDs and reaction wheels), $\boldsymbol{\tau}_b$ is the combined disturbance torques on the spacecraft, $\boldsymbol{\omega}$ is the angular velocity of the spacecraft in ICRF, and I is the spacecraft inertia tensor matrix.

2.3 External Forces

Solar Radiation Pressure Force

The SRP force (\mathbf{F}_{SRP}) is dependent on the reflectivity of the sail surface. Assuming a flat surface, the force is the sum of the forces produced by the light that is specularly reflected (\mathbf{F}_s), diffusively reflected (\mathbf{F}_d), and absorbed (\mathbf{F}_a) [15].

The specular reflection force (\mathbf{F}_s) is represented by [15]:

$$\mathbf{F}_s = -2\rho_s P_{srp} A \cos^2(\phi) \hat{\mathbf{n}}, \quad (4)$$

where ρ_s is the rate of specular reflection, P_{srp} is the solar radiation pressure, A is the reflective area, $\hat{\mathbf{n}}$ is the unit vector normal to the solar sail plane, and ϕ is the angle between $\hat{\mathbf{n}}$ and the sun-spacecraft unit vector ($\hat{\mathbf{r}}_s$).

The diffusive reflection force (\mathbf{F}_d) is represented by [15]:

$$\mathbf{F}_d = \rho_d P_{srp} A |\cos(\phi)| \left(\hat{\mathbf{r}}_s - \frac{2}{3} \hat{\mathbf{n}} \right), \quad (5)$$

where ρ_d is the rate of diffusive reflection. The absorption force (\mathbf{F}_a) is represented by [15]:

$$\mathbf{F}_a = \rho_a P_{srp} A |\cos(\phi)| \hat{\mathbf{r}}_s, \quad (6)$$

where ρ_a is the rate of absorption. The rates of specular reflection, diffusive reflection and absorption satisfy the condition $\rho_s + \rho_d + \rho_a = 1$. P_{srp} is given by:

$$P_{srp} = \frac{S}{c}, \quad (7)$$

where S is the solar constant and c is the speed of light. A dual cone eclipse shadow model is used to adjust the SRP force when the spacecraft is eclipsed by the Earth or Moon.

Atmospheric Drag Force

The atmospheric drag force (\mathbf{F}_{drag}) was calculated using the following [14]:

$$\mathbf{F}_{drag} = -\frac{1}{2}\rho C_d A_{ram} |\mathbf{v}_{rel}|^2 \hat{\mathbf{v}}_{rel}, \quad (8)$$

where ρ is the air density, C_d is the drag coefficient, A_{ram} is the ram (frontal) area of the satellite, \mathbf{v}_{rel} is the velocity relative to the atmosphere, and $\hat{\mathbf{v}}_{rel}$ is the unit vector of \mathbf{v}_{rel} . The NRLMSISE-00 atmosphere model was used to generate air density values. A_{ram} is given by:

$$A_{ram} = |A \cos(\psi)|, \quad (9)$$

where A is the area of the solar sail and ψ is the angle between $\hat{\mathbf{v}}_{rel}$ and $\hat{\mathbf{n}}$. Due to the relative size of the satellite bus, only the solar sail area is considered for the atmospheric drag. \mathbf{v}_{rel} is calculated by using the difference between the atmosphere velocity (\mathbf{v}_{atm}) and the satellite velocity in ICRF, before converting to the body-frame. Since the atmosphere is assumed to rotate with the Earth, \mathbf{v}_{atm} is given by [16]:

$$\mathbf{v}_{atm} = \cos(\mu) \boldsymbol{\omega}_{Earth} \times \mathbf{X}_{ICRF}, \quad (10)$$

where $\boldsymbol{\omega}_{Earth}$ is the angular velocity vector of the Earth, μ is the latitude of the satellite and \mathbf{X}_{ICRF} is the radial vector of the satellite from Earth in ICRF.

2.4 Disturbance Torques

Solar Radiation Pressure Torque

The SRP torque ($\boldsymbol{\tau}_{srp}$) is calculated using [14]:

$$\boldsymbol{\tau}_{srp} = \mathbf{c}_s \times \mathbf{F}_{srp}, \quad (11)$$

where \mathbf{c}_s is the vector from the satellite centre of mass to the SRP centre of pressure.

Atmospheric Drag Torque

The atmospheric drag torque ($\boldsymbol{\tau}_{drag}$) is calculated using [14]:

$$\boldsymbol{\tau}_{drag} = \mathbf{c}_a \times \mathbf{F}_{drag}, \quad (12)$$

where \mathbf{c}_a is the vector from the satellite centre of mass to the aerodynamic centre of pressure.

Magnetic Field Torque

The magnetic field torque ($\boldsymbol{\tau}_M$) is calculated using [14]:

$$\boldsymbol{\tau}_M = \mathbf{M} \times \mathbf{B}_b, \quad (13)$$

where \mathbf{M} is the residual dipole of the satellite, and \mathbf{B}_b is the Earth's magnetic field vector in the body-frame. The World Magnetic Model 2020 is used to calculate the Earth's magnetic field vector in the North-East-Down (NED) reference frame. This is converted to the ECI frame using:

$$\mathbf{B}_{ECI} = DCM_{ECI}(DCM_{ECEF} \mathbf{B}_{NED}), \quad (14)$$

where \mathbf{B}_{ECI} , \mathbf{B}_{NED} are the Earth's magnetic field vectors in the ECI and NED frames respectively, and DCM_{ECI} , DCM_{ECEF} are the Direction Cosine Matrices converting from ECEF to ECI frame and from NED to ECEF frame, respectively. The ECI frame is treated as

equivalent to ICRF. \mathbf{B}_{ECI} is converted to the spacecraft body frame using quaternion rotation [17]:

$$\mathbf{B}_b = q^{-1} \otimes \left[\frac{0}{\mathbf{B}_{ECI}} \right] \otimes q, \quad (15)$$

where q is the satellite attitude quaternion, and \otimes is the operator of a quaternion multiplication.

Gravity Gradient Torque

The gravity gradient torque (τ_{GG}) is calculated using [18]:

$$\tau_{GG} = \frac{3\mu_{\oplus}}{|\mathbf{X}|^3} \hat{\mathbf{X}} \times I \hat{\mathbf{X}}, \quad (16)$$

where μ_{\oplus} is the geocentric gravitational constant, I is the inertia tensor of the spacecraft, \mathbf{X} is the spacecraft position vector, and $\hat{\mathbf{X}}$ is the unit vector of \mathbf{X} .

2.5 Reaction Wheels

Theory and Modelling

Ignoring friction, the reaction wheel torque is equal in magnitude and opposite in direction to the spacecraft torque so that:

$$\tau_{SC} = -\tau_{RW}, \quad (17)$$

where τ_{SC} and τ_{RW} are the spacecraft torque and reaction wheel torque, respectively.

The reaction wheel angular velocity is calculated based on the desired torque signal from the reaction wheel controller, using the following formula [19]:

$$\omega_f = \omega_i - \frac{\tau_{des}}{I_w} dt, \quad (18)$$

where ω_f, ω_i are the final and initial wheel angular velocities respectively, τ_{des} is the desired spacecraft torque, I_w is the moment of inertia of the reaction wheel, and dt is the timestep.

The reaction wheel is assumed to be a rotor with a solid disk. The moment of inertia (I_w) was calculated with the following equation:

$$I_w = \frac{1}{2} m R^2, \quad (19)$$

where m and R are the mass and radius of the reaction wheel rotor, respectively.

The peak momentum (h_{\max}) was used to calculate the maximum angular velocity (ω_{\max}) using:

$$\omega_{\max} = \frac{h_{\max}}{I_w} \quad (20)$$

The reaction wheel momentum is therefore limited between $[-\omega_{\max}, \omega_{\max}]$. The torque output on the spacecraft (τ_{SC}) is calculated from this limited value (ω_{lim}) using:

$$\tau_{SC} = -\frac{\omega_{lim} - \omega_i}{dt} I_w \quad (21)$$

Control Law

Given the desired quaternion spacecraft attitude (q_{des}) and the current quaternion spacecraft attitude (q_t), the error is given by:

$$q_{error} = q_{des} - q_t \quad (22)$$

As q_{error} is a unit quaternion, its Direct-Cosine-Matrix (DCM) is defined as [17]:

$$DCM = \begin{bmatrix} (q_0^2 + q_1^2 - q_2^2 - q_3^2) & 2(q_1q_2 + q_0q_3) & 2(q_1q_3 - q_0q_2) \\ 2(q_1q_2 - q_0q_3) & (q_0^2 - q_1^2 + q_2^2 - q_3^2) & 2(q_2q_3 + q_0q_1) \\ 2(q_1q_3 + q_0q_2) & 2(q_2q_3 - q_0q_1) & (q_0^2 - q_1^2 - q_2^2 + q_3^2) \end{bmatrix}, \quad (23)$$

where q_0 is the scalar component of q_{error} , and q_1, q_2, q_3 are the vector components of q_{error} . The corresponding rotation angles for an XYZ rotation order are defined as [17]:

$$\phi = \text{atan2}(DCM(2,3), DCM(3,3)), \quad (24)$$

$$\theta = -\text{asin}(DCM(1,3)), \quad (25)$$

$$\psi = \text{atan2}(DCM(1,2), DCM(1,1)), \quad (26)$$

where ϕ, θ , and ψ are the rotation angles about the X, Y, and Z axes, respectively. The rotation angle error (\mathbf{e}) is given by:

$$\mathbf{e} = \begin{pmatrix} \phi \\ \theta \\ \psi \end{pmatrix} \quad (27)$$

The control torque output for the PD controller, commonly used for satellite attitude control, is given by:

$$\tau_{des} = K_p \mathbf{e} + K_d \dot{\mathbf{e}}, \quad (28)$$

where K_p, K_d are the proportional and derivative coefficients, respectively, and $\dot{\mathbf{e}}$ is the time derivative of \mathbf{e} .

Implementation

Three reaction wheels were modelled in an orthogonal configuration, aligned with the x, y, and z axes of the satellite body. The model is based on RocketLab's RW-0.01 reaction wheel [20], which is said to be suitable for smaller CubeSats. The mass and radius of the rotor were assumed to be 90% of the total mass and housing radius of the reaction wheel. ω_{max} was set to 1017 rad/s based on the reaction wheel h_{max} from [20]. Gain scheduling was implemented for K_p and K_d , so that their values vary depending on the error, allowing for better control over a larger range of errors. The lookup table is shown in Table 1.

Table 1. Lookup table for PD controller coefficients

$\ \mathbf{e}\ ^2$	K_p	K_d
7.5×10^{-3}	4×10^{-4}	4×10^{-2}
3×10^{-2}	6×10^{-5}	3×10^{-2}

$\|\mathbf{e}\|^2$ is the squared norm of the error. Linear interpolation is used to transition between K_p and K_d values. These values were chosen to avoid overshoot for large errors and reduced steady-state error when small errors are present. The PD controller output is limited to ± 1.0 mNm as the reaction wheel actuators are limited in their torque output [20].

2.6 Reflectivity Control Devices

Theory and Modelling

The reflectivity control devices (RCDs) provide torques by setting RCDs along one edge of the solar sail to be specular reflection dominant and the opposite edge to be diffusive reflection dominant. Since generally more force is produced for specular reflection than diffusive reflection [21], a force imbalance is present, and a torque is generated.

The specular reflection, diffusive reflection and absorption force are modelled using Eq. 4, 5, and 6. When an RCD is ON, the reflection/absorption rates (ρ_s, ρ_d, ρ_a) change so that specular reflection is dominant, producing a force \mathbf{F}_{ON} . When an RCD is OFF, the reflection/absorption rates (ρ_s, ρ_d, ρ_a) change so that diffusive reflection is dominant, producing a force \mathbf{F}_{OFF} . When two RCDs are positioned on the solar sail a distance $-d$ and d from the centre of mass, and each side is set to different states, the torque ($\boldsymbol{\tau}_{RCD}$) is given by:

$$\boldsymbol{\tau}_{RCD} = \mathbf{d}_1 \times \mathbf{F}_{ON} \hat{\mathbf{n}} + \mathbf{d}_2 \times \mathbf{F}_{OFF} \hat{\mathbf{n}}, \quad (29)$$

where \mathbf{d}_1 and \mathbf{d}_2 are 3x1 vectors representing the distance between each RCD and the spacecraft centre of mass in the body-frame. Since the RCDs are located on opposite sides of the sail, $\mathbf{d}_1 = -\mathbf{d}_2$.

Control Law

During sun-pointing mode, the RCD controller is given the reaction wheel X and Y angular velocities (ω_{RW_X} and ω_{RW_Y}). To offload momentum from the reaction wheels, a torque must be produced according to the following:

$$\boldsymbol{\tau}_{RCD_X}(\omega_{RW_X}) = \begin{cases} \boldsymbol{\tau}_{RCD} & \omega_{RW_X} > 0 \\ -\boldsymbol{\tau}_{RCD} & \omega_{RW_X} < 0 \end{cases}, \quad (30)$$

$$\boldsymbol{\tau}_{RCD_Y}(\omega_{RW_Y}) = \begin{cases} \boldsymbol{\tau}_{RCD} & \omega_{RW_Y} > 0 \\ -\boldsymbol{\tau}_{RCD} & \omega_{RW_Y} < 0 \end{cases}, \quad (31)$$

where $\boldsymbol{\tau}_{RCD_X}$ and $\boldsymbol{\tau}_{RCD_Y}$ are the torque produced by the RCDs about the X and Y axis, respectively.

Implementation

Sun-pointing mode is initiated once a reaction wheel speed of 700 rad/s ($\sim 0.7\omega_{\max}$) has been reached.

The reflection/absorption rates for both RCD ON and RCD OFF states are summarised in Table 2 based on values presented in [22].

Table 2. Summary of reflection/absorption rates

RCD State	ρ_s	ρ_d	ρ_a
ON	0.5	0.3	0.2
OFF	0.1	0.5	0.4

Due to the configuration of the RCDs shown in Fig. 3, RCD2 and RCD4 are commanded to offload momentum from reaction wheel X (aligned with body x-axis), and RCD1 and RCD3 are commanded to offload momentum from reaction wheel Y (aligned with body y-axis).

Hysteresis control was implemented to avoid rapidly turning the RCDs on and off. If the reaction wheel speed exceeds a magnitude of 100 rad/s, momentum offloading occurs. When the wheel speed is reduced to 50 rad/s, momentum offloading ceases, preventing overshoot from occurring. Because these values are sufficiently spaced, oscillations from rapid

transitioning between states is avoided. Four S-R Flip Flops are used to store the current state of each RCD. The hysteresis implementation is summarised in Table 3 and Table 4.

Table 3. RCD1 and RCD3 truth table

	RCD1	RCD3
$\omega_{RW_Y} > 100$	SET ON	SET OFF
$-50 < \omega_{RW_Y} < 50$	SET OFF	SET OFF
$\omega_{RW_Y} < -100$	SET OFF	SET ON
Else	HOLD STATE	HOLD STATE

Table 4. RCD2 and RCD4 truth table

	RCD2	RCD4
$\omega_{RW_X} > 100$	SET OFF	SET ON
$-50 < \omega_{RW_X} < 50$	SET OFF	SET OFF
$\omega_{RW_X} < -100$	SET ON	SET OFF
Else	HOLD STATE	HOLD STATE

Once both reaction wheel X and reaction wheel Y have been slowed below 100 rad/s, the satellite returns to Earth-pointing mode and the RCDs are no longer used.

3 Numerical Simulation

3.1 Model Parameters

The models were implemented in Simulink using the Aerospace Blockset. A fixed timestep of 30 seconds was used with a Bogacki-Shampine (ode3) solver. Sensitivity analysis was conducted to determine the appropriate timestep. Spacecraft properties from the LightSail 2 mission [23] were used and are summarised in Table 5 below.

Table 5. Spacecraft properties

Description	Value	Units
Mass	4.93	kg
Moments of Inertia I_{xx}, I_{yy}, I_{zz}	3.79, 3.79, 7.33	kg m ²
Products of Inertia I_{xy}, I_{yz}, I_{xz}	$-1.90 \times 10^{-4}, -8.18 \times 10^{-4}, 1.47 \times 10^{-3}$	kg m ²
Sail Area	32	m ²
Satellite Bus Dimensions	$0.3 \times 0.1 \times 0.1$	m
Drag Coefficient (C_d)	2.2	

The initial satellite orbital parameters were chosen for a 700km Sun-synchronous orbit. These are provided in Table 6.

Table 6. Initial satellite orbital parameters

Description	Value	Units
Epoch	July 11 th , 2024	
Semi-major Axis	7 078 140	m
Eccentricity	0.001	
Inclination	98.1928	°
RAAN	22	°
Argument of Periapsis	0	°
True Anomaly	0	°

The sail is assumed to have a total reflectivity of 0.9 and a specular reflectivity fraction of 0.89 from optical testing conducted by NASA [24]. This translates to a specular reflection rate (ρ_s) of 0.81, diffusive reflection rate (ρ_d) of 0.1, and an absorption rate (ρ_a) of 0.09 assuming no transmission. Other key parameters are summarised in Table 7.

Table 7. Additional spacecraft properties

Description	Value	Units
CoM – Aerodynamic CoP (\mathbf{c}_a)	$[0, 0, -0.15]^T$	m
CoM – SRP CoP (\mathbf{c}_s)	$[0.01, 0.01, -0.15]^T$	m
Spacecraft residual dipole (\mathbf{M})	$[2.8868, 2.8868, 2.8868]^T \times 10^{-4}$	Am^2

3.2 Model A

The results for the Model A spacecraft (no RCDs) are shown below. Fig. 6 displays the rotation angles of the spacecraft in the LVLH frame and Fig. 7 displays the angular velocity of the three reaction wheels.

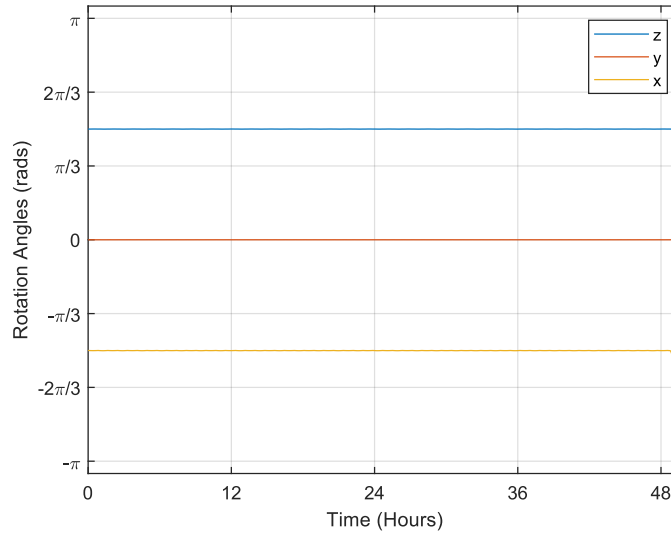


Figure 6. Model A LVLH to body-frame rotation angles. Rotations are conducted in the order of Z (blue), Y (orange), X (yellow).

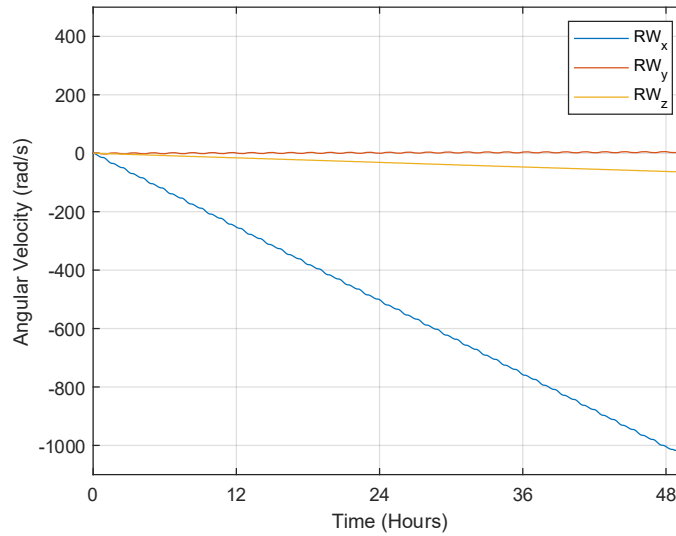


Figure 7. Model A reaction wheel angular velocities for reaction wheel X (blue), reaction wheel Y (orange), and reaction wheel Z (yellow)

Fig. 6 demonstrates the successful implementation of the control system, while Fig. 7 shows that saturation of reaction wheel X occurs shortly after 48 hours when an angular velocity of -1017 rad/s is reached. Ignoring the time after saturation occurs, the maximum rotation error in each axis (X, Y, Z) is $[5.59, 4.94, 1.11] \times 10^{-5}$ radians. A combined maximum pointing error of 3.08×10^{-3} radians was found using the square root of the sum of the squares of the individual errors. When saturation occurs, 3-axis control of the spacecraft is lost, and the spacecraft starts to rotate.

The X-axis experiences the largest disturbance torques, evident from the build-up of momentum in reaction wheel X. This is largely due to the SRP disturbance torques which measure up to nearly 1.2×10^{-6} Nm in the X-axis. Meanwhile, atmospheric drag torques, which largely affect the Y-axis of the spacecraft body, are only measured to be in the order of 10^{-8} Nm. Magnetic field torque is similarly measured to be in the order of 10^{-8} Nm. Gravity gradient torque is implemented separately using the ‘Spacecraft Dynamics’ [12] block and is therefore not measured.

While the X and Z axes experience bias disturbance torques (net torque), the Y-axis experiences mostly zero net torque disturbances resulting from torques balancing out over time. The angular velocity of reaction wheel Y therefore does not deviate far from 0. These results demonstrate that using reaction wheels for solar sail attitude control without additional actuators is ineffective due to the bias disturbance torques, which leads to reaction wheel saturation.

3.3 Model B

The results for the Model B spacecraft (with RCDs) are shown below. Fig. 8 displays the rotation angles of the spacecraft in the LVLH frame and Fig. 9 displays the angular velocity of the three reaction wheels. Fig. 10 shows the torque generated from the RCDs during the offloading period.

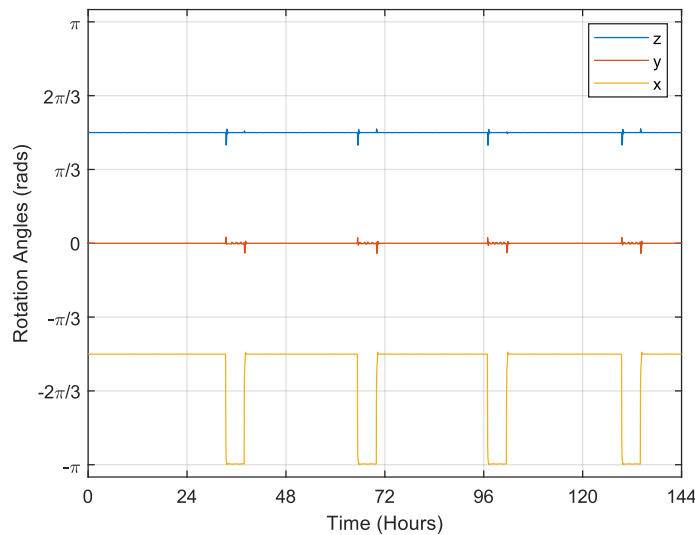


Figure 8. Model B LVLH to body-frame rotation angles. Rotations are conducted in the order of Z (blue), Y (orange), X (yellow).

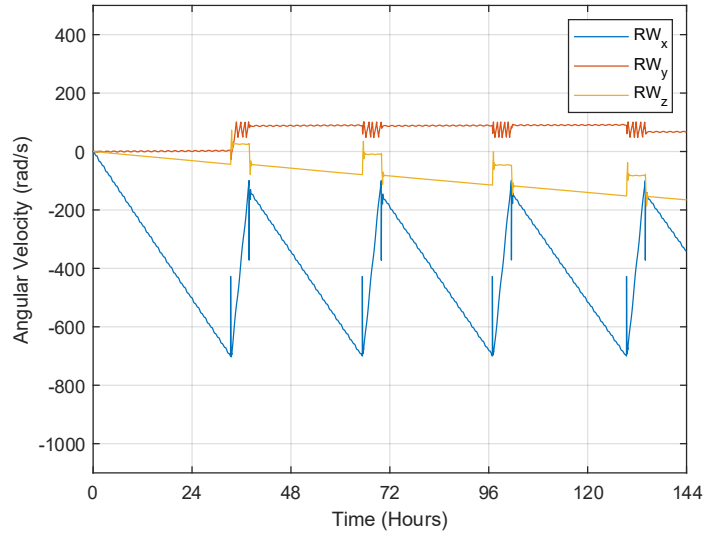


Figure 9. Model B reaction wheel angular velocities for reaction wheel X (blue), reaction wheel Y (orange), and reaction wheel Z (yellow).

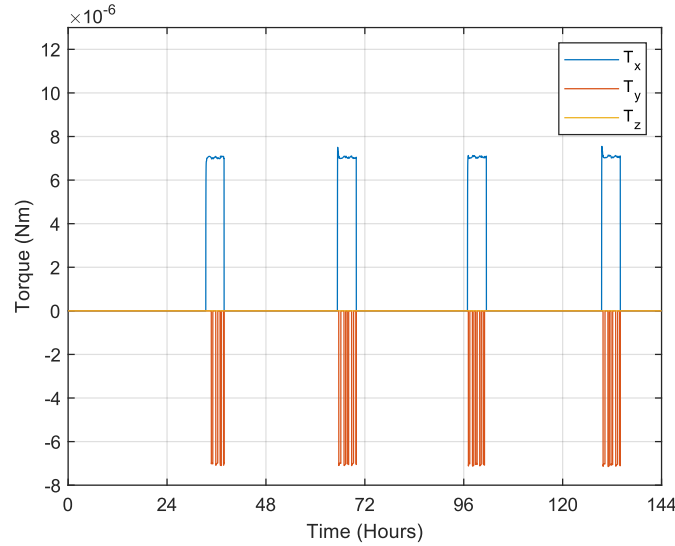


Figure 10. Model B total RCD torques produced along the body X-axis (blue), Y-axis (orange), and Z-axis (yellow).

A six-day period was simulated to assess the momentum offloading capabilities of the RCDs. Fig. 9 shows that momentum offloading occurred four times during the simulation. Sun-pointing mode lasted between 4 hours and 29 minutes and 4 hours and 37 minutes running for 12.66% of the total simulated time. When commanded to be sun pointing, rotation was typically conducted within 12 minutes to within 10° of the target position.

Fig. 9 shows that momentum was offloaded from both reaction wheel X and reaction wheel Y. Y-axis disturbance torques increase during the sun-pointing orientation because of greater y-axis atmospheric drag torque (up to 1.1×10^{-6} Nm) and SRP torque (up to 3.6×10^{-6} Nm). The RCDs are therefore used periodically to overcome these disturbances as shown in Fig. 10. The atmospheric drag torque increases in sun-pointing mode as sun-pointing is prioritised over aerodynamics, resulting in a larger ram area of the sail. A torque of up to 7.6×10^{-6} Nm is produced from the RCDs and varies depending on the angle between the solar sail normal and the sun-satellite vector.

While the RCDs successfully demonstrate their momentum offloading capabilities, preventing saturation of reaction wheel X and Y, reaction wheel Z does increase in angular velocity over time. This momentum cannot be offloaded using RCDs and will eventually require additional actuators like magnetorquers or thrusters. However, saturation of reaction wheel Z is estimated to take more than 30 days from extrapolation.

3.4 Sensitivity Analysis

Due to uncertainty in some of the parameters, particularly those listed in Table 7, a sensitivity analysis was performed to assess how varying key parameters changes the results. These parameters were chosen as they were not found directly in previous literature or expected to alter the results.

Timestep

A timestep of 30 seconds was used for the simulations as it was noted that the results were similar to that of 10 seconds and 1 second timesteps for shorter intervals. Timesteps greater than 60 seconds resulted in discrepancies in the angular velocities of the reaction wheels and therefore were not used.

Residual Dipole

The residual dipole of the spacecraft was chosen so that $\|\mathbf{M}\| = 5 \times 10^{-4} \text{ Am}^2$ corresponding to the estimated residual dipole of the 3U Pace CubeSat [25]. However, [14] says that a residual dipole of the order $\|\mathbf{M}\| = 0.1 \text{ Am}^2$ is typical. This indicates a large range in values. When using the latter value in the simulations, the magnetic field torque becomes the dominant torque during nominal Earth-pointing, increasing the momentum offloading required (five times in 6 days). Some pointing accuracy is also lost due to the increase in disturbance torques.

Centre of Pressure

Both the centre of atmospheric drag pressure (\mathbf{c}_a) and the centre of the SRP (\mathbf{c}_s) can vary depending on the spacecraft and sail properties. [26] considers a solar sail with a centre of mass to centre of SRP offset 0.25% of the sail length. Therefore, for a 5.6 x 5.6m solar sail an offset of magnitude 1.41 cm along the sail plane was used. Increasing the centre of pressure offset for both \mathbf{c}_a and \mathbf{c}_s to 5 cm in magnitude greatly increases the disturbance torques on the spacecraft. The SRP disturbance torque is most significant during sun-pointing producing torques up to 10^{-5} Nm . This is the result of larger SRP force produced when fully illuminated by the sun. As this torque is greater than the torque capabilities of the RCDs, momentum offloading is unsuccessful, and saturation of the reaction wheels becomes inevitable. This result demonstrates the importance of minimising the SRP centre of pressure deviation along the solar sail plane. As the centre of pressure deviation is heavily dependent on manufacturing and deployment success, it is difficult to determine a realistic value. The significance of this value cannot be overstated and the success of the model implementation is heavily dependent on this.

RCD Reflectivity Rates

Even with slightly modified reflectivity rates so that the RCDs have lower performance (50% increase in absorption rate when ON), the RCDs can still be utilised to offload momentum. Torques produced are up to $4.8 \times 10^{-6} \text{ Nm}$ and momentum offloading time is greatly increased (~9 hours).

3.5 Model Validation

[5] reported that LightSail 2 required daily momentum offloading to prevent saturation of the reaction wheel. This aligns well with these results as momentum offloading is conducted four times in six days. However, the LightSail 2 mission required frequent slews and made use of 1 reaction wheel with 3 magnetorquers so a direct comparison is difficult to make.

[22] provides RCD torque capabilities for different sail lengths between 10 and 300 metres. Using cubic extrapolation, a torque for a 5.66m length solar sail is expected to be $\sim 6 \times 10^{-6}$ Nm in magnitude. This aligns relatively closely to the measured torque of 7.6×10^{-6} Nm, indicating that the RCD torque values are reasonable.

3.6 Limitations and Assumptions

The solar flux used for solar radiation pressure calculations is assumed to be a constant 1367 W/m^2 . In reality, this value fluctuates, although it is commonly assumed to be constant in literature. In all calculations, the spacecraft bus is neglected due to its small size relative to the sail and difficulty to model. This is expected to increase SRP and atmospheric drag torques slightly. The solar sail is assumed to be a rigid body with no wrinkles, tears or inconsistencies. While the reflection/absorption rates account for some of this, results are likely to vary depending on surface conditions. The atmosphere is assumed to be rotating with the Earth, which is a great simplification, but reasonable in some cases. The reaction wheels are assumed to be perfect actuators, providing instantaneous torque with no inefficiencies. The position and attitude of the spacecraft are known exactly with results expected to vary due to sensor noise and inaccuracies.

This model is limited in that it only considers a short six-day period of a specific orbit. Performance over longer periods of time and varying orbits is uncertain. Limited real-world data has been used for verification so results may not represent real-world outcomes.

3.7 Implications

These results indicate the potential application of RCDs for offloading momentum from reaction wheels during solar sailing in a low-Earth orbit. While magnetorquers have historically been used for this purpose [6], RCDs could additionally be used to simplify control and reduce spacecraft tumbling. This result also indicates additional future applications for RCDs in high-orbit or deep space solar sail missions where magnetorquers cannot be used. Since maximum torque from the RCDs is produced when the sail normal and sun-spacecraft vector align, the inclusion of two distinct modes (Earth-pointing and Sun-pointing) proved to be appropriate. This maximised the time spent in nominal Earth observation by decreasing the momentum offloading period. Reducing atmospheric drag during nominal operations also proved to be significant for reducing disturbance torques and should be considered in future missions.

Further investigation should be conducted into the disturbance torques created from the spacecraft bus. A non-rigid sail should also be modelled as disturbance torques and non-ideal solar sailing performance is expected. Sensors and more realistic actuators should also be implemented, which could increase pointing error and as a result, increase disturbance torques. Additional disturbances are significant as they may affect momentum offloading if their magnitudes exceed the torque capabilities of the RCDs. Additional orbits and spacecraft properties should also be tested to determine other possible applications for RCDs. While solar sails with RCDs are identified to be feasible, specific missions or objectives have not been identified and should therefore be investigated.

4 Conclusion

Solar sailing utilises SRP to generate thrust instead of traditional propulsion systems. This has been successfully demonstrated in JAXA's IKAROS mission and the LightSail 2 mission. IKAROS first demonstrated the capabilities of RCDs to generate torques and perform attitude control. LightSail 2 demonstrated solar sailing in an Earth orbit but suffered from frequent saturation of its reaction wheel due to the large mass moment of inertia associated with solar sails. To prevent this, RCDs are proposed as a method of periodically offloading the reaction wheel momentum, allowing for continuous control throughout the mission.

Two models were developed to assess this: Model A - a solar sail with three orthogonal reaction wheels, and Model B - a solar sail with three orthogonal reaction wheels and RCDs. Orbital and attitude dynamics were modelled alongside SRP, atmospheric drag, magnetic field and gravity gradient disturbance torques. Numerical simulation was conducted using a custom-built program, developed with Simulink's Aerospace Blockset. A 700km sun-synchronous orbit was chosen for a spacecraft with similar properties to that of LightSail 2. In Model A, saturation of the reaction wheels occurred shortly after 48 hours. Model B demonstrated by alternating between nominal Earth pointing and Sun-pointing (for maximising RCD torque), successful momentum offloading of the X and Y-aligned reaction wheels. The Z-aligned reaction wheel cannot be offloaded using RCDs and is expected to become saturated after 30 days.

Sensitivity analysis of some key parameters was performed to assess the robustness of the model, and its limitations are stated. RCDs are a viable solution for reaction wheel saturation when used in conjunction with additional actuators and carry little risk due to their flight heritage. Investigation should be conducted into specific missions and applications for this technology to identify where the most value can be added.

Acknowledgements

I would like to acknowledge my supervisor Dr. Yang Yang for his support throughout this project. Additionally, I would like to thank the team at the Geo-Informatics and Space Technology Development Agency (GISTDA) in Bangkok, Thailand for hosting me and providing an introduction into spacecraft attitude and control systems. Thank you to Connor Boughton for his support in developing the models.

Reference

- [1] S. R. Starin and J. Eterno, "Attitude determination and control systems," 2011.
- [2] R. L. Garwin, "Solar sailing-a practical method of propulsion within the solar system," vol. 28, ed: AMER INST AERONAUT ASTRONAUT 1801 ALEXANDER BELL DRIVE, STE 500, RESTON, VA ..., 1958, pp. 188-190.
- [3] Y. Tsuda *et al.*, "Achievement of IKAROS—Japanese deep space solar sail demonstration mission," *Acta Astronautica*, vol. 82, no. 2, pp. 183-188, 2013.
- [4] Y. Tsuda *et al.*, "Flight status of IKAROS deep space solar sail demonstrator," *Acta astronautica*, vol. 69, no. 9-10, pp. 833-840, 2011.
- [5] D. A. Spencer, B. Betts, J. M. Bellardo, A. Diaz, B. Plante, and J. R. Mansell, "The LightSail 2 solar sailing technology demonstration," *Advances in Space Research*, vol. 67, no. 9, pp. 2878-2889, 2021.
- [6] J. Mansell *et al.*, "Orbit and attitude performance of the LightSail 2 solar sail spacecraft," in *AIAA Scitech 2020 Forum*, 2020, p. 2177.
- [7] M. Berthet and K. Suzuki, "Sunflower mission concept for high-altitude earth observation in LEO via nanosatellite with pyramidal solar sail," *Acta Astronautica*, vol. 213, pp. 516-536, 2023.

- [8] V. Lappas *et al.*, "CubeSail: A low cost CubeSat based solar sail demonstration mission," *Advances in Space Research*, vol. 48, no. 11, pp. 1890-1901, 2011.
- [9] B. Fu, E. Sperber, and F. Eke, "Solar sail technology—A state of the art review," *Progress in Aerospace Sciences*, vol. 86, pp. 1-19, 2016.
- [10] T. Friesen. "NASA Next-Generation Solar Sail Boom Technology Ready for Launch." NASA. <https://www.nasa.gov/general/nasa-next-generation-solar-sail-boom-technology-ready-for-launch/> (accessed 16/07/2024, 2024).
- [11] J. Orphee, B. Diedrich, B. Stiltner, C. Becker, and A. Heaton, "Solar sail attitude control system for the NASA near earth asteroid Scout mission," in *International Symposium on Solar Sailing*, 2017, no. M17-5741.
- [12] "Spacecraft Dynamics." MathWorks. <https://se.mathworks.com/help/aeroblks/spacecraftdynamics.html> (accessed 18th April, 2025).
- [13] L. Boldt-Christmas. "Polar and Sun-synchronous orbit." The European Space Agency. https://www.esa.int/ESA_Multimedia/Images/2020/03/Polar_and_Sun-synchronous_orbit (accessed 17/07/2024, 2024).
- [14] W. J. Larson and J. R. Wertz, "Space mission analysis and design," 1999.
- [15] A. Farres, "Propellant-less systems," in *Next Generation CubeSats and SmallSats*, F. Branz, C. Cappelletti, A. J. Ricco, and J. W. Hines Eds.: Elsevier, 2023, ch. 21, pp. 519-541.
- [16] J. Southard. "7.2: The Coriolis Effect on the Earth's Surface " LibreTexts. [https://geo.libretexts.org/Bookshelves/Sedimentology/Introduction_to_Fluid_Motions_and_Sediment_Transport_\(Southard\)/07%3A_Flow_in_Rotating_Environments/7.02%3A_The_Coriolis_Effect_on_the_Earth's_Surface](https://geo.libretexts.org/Bookshelves/Sedimentology/Introduction_to_Fluid_Motions_and_Sediment_Transport_(Southard)/07%3A_Flow_in_Rotating_Environments/7.02%3A_The_Coriolis_Effect_on_the_Earth's_Surface) (accessed April 18 2025).
- [17] J. Diebel, "Representing attitude: Euler angles, unit quaternions, and rotation vectors," *Matrix*, vol. 58, no. 15-16, pp. 1-35, 2006.
- [18] S. A. Rawashdeh, "Attitude Analysis of Small Satellites Using Model-Based Simulation," *International Journal of Aerospace Engineering*, vol. 2019, no. 1, p. 3020581, 2019.
- [19] D. Sinclair and C. Grant, "Reaction Wheel," ed: RocketLab, 2021.
- [20] RocketLab, "Reaction Wheel," in *RW-0.01 Data Sheet*, ed: RocketLab, 2024.
- [21] R. Funase *et al.*, "On-orbit verification of fuel-free attitude control system for spinning solar sail utilizing solar radiation pressure," *Advances in Space Research*, vol. 48, no. 11, pp. 1740-1746, 2011.
- [22] S. Kikuchi and J. i. Kawaguchi, "Asteroid de-spin and deflection strategy using a solar-sail spacecraft with reflectivity control devices," *Acta Astronautica*, vol. 156, pp. 375-386, 2019.
- [23] J. R. Mansell, J. M. Bellardo, B. Betts, B. Plante, and D. A. Spencer, "LightSail 2 solar sail control and orbit evolution," *Aerospace*, vol. 10, no. 7, p. 579, 2023.
- [24] B. M. Gauvain and D. A. Tyler, "A solar sail shape modeling approach for attitude control design and analysis," in *6th International Symposium on Space Sailing (ISSS)*, 2023.
- [25] J. Springmann, J. Cutler, and H. Bahcivan, "Magnetic sensor calibration and residual dipole characterization for application to nanosatellites," in *AIAA/AAS Astrodynamics Specialist Conference*, 2010, p. 7518.
- [26] B. Wie, "Dynamic Modeling and Attitude Control of Solar Sail Spacecraft: Part I," *American Institute of Aeronautics and Astronautics*, 2002.